

# Artificial Tendons Improve Fault-Tolerance of Robotic Arms Under Free-Swinging Failures

Qiang Yue  
 Division of Mechanics  
 Beijing Computational Science  
 Research Center  
 Beijing, China  
 yq1998@csrc.ac.cn

Yang Ding\*  
 Division of Mechanics  
 Beijing Computational Science  
 Research Center  
 Beijing, China  
 dingyang@csrc.ac.c  
 \*Corresponding author

**Abstract**—In hazardous environments, the deployment of robotic arms that can withstand failures without compromising task performance is crucial. This paper focuses on enhancing the fault tolerance of robotic arms, specifically addressing free-swinging failures, which have been less explored compared to locked-joint failures in prior studies. To mitigate the impact of free-swinging failures, a novel fault-tolerance structure is proposed, incorporating artificial tendons (elastic strings) along both sides of the robotic arm segments. These artificial tendons are designed to generate torques at the joints in the event of a failure, enabling the robotic arm to retain its ability to move within certain regions of the workspace, defined as the fault-tolerant workspace (FTWS). Comparative analysis in both planar and spatial scenarios demonstrates that the robotic arm equipped with artificial tendons exhibits a significantly larger FTWS than one relying solely on locking the failed joint, provided that a free-swinging failure is detected. The findings from this research present innovative avenues for the design and development of fault-tolerant robotic arms.

**Keywords**—*fault tolerance, free-swinging failure, artificial tendon, robotic arm*

## I. INTRODUCTION

Robots find applications in diverse fields such as medicine [1], outer space [2], deep-sea exploration [3], nuclear industries [4], and other unstructured or hazardous environments, where their usage mitigates human exposure to danger. Despite their crucial role, robots operating in severe conditions often experience high failure rates, leading to a substantial reduction in availability, plummeting to as low as 50% [5], [6]. The development of fault-tolerant robotic arms, capable of performing tasks even in the presence of component failures, is of significant practical interest.

Joint failures of robotic arms typically manifest in two main forms: locked-joint failure and free-swinging failure [7]. Locked-joint failures, caused by issues such as motor brakes and transmission mechanism jamming, can be actively induced to isolate the impact of faults [8]. Current research on fault-tolerant robotic arms predominantly focuses on addressing locked-joint failures, emphasizing model reconstruction [9], fault-tolerant performance evaluation [10], and fault-tolerant motion planning [11]. In addition, high-frequency excitation and a failed motor can lead to free-swinging failure [12], [13]. Recovery methods

for free-swinging failures often involve locking the joints, converting them into locked-joint faults [14]. In scenarios where the free-swinging failure joint remains unlocked, external forces, such as gravity, are required to make the pose of the robotic arm predictable [15].

A commonly used measure of fault tolerance of a robotic arm is the size of its fault-tolerant workspace (FTWS). The first-order FTWS is defined as the intersection of positions reachable by the end effector under any single joint failure [16]. For robotic arms with locked-joints failure, where the angle of the failure joint is unknown, it becomes imperative to consider the all angles at which the failure joint may be locked. Previous studies showed that a planar robotic arm needs 4 joints to ensure non-zero FTWS [16]. In contrast, for free-swinging robotic arms, the failure joint can continue moving after the failure, relying on external force and torque. Over time, the failure joint reaches a stable angle where the actuator torque becomes zero, serving as a parameter for calculating the FTWS [17]. The gravity is considered as an external force in [17], where the zero-torque inverse kinematics problem for a three-link planar robotic arm is solved and the FTWS of a planar region symmetric along the direction of gravity is derived. This distinction in calculation methods allows a nuanced evaluation of fault tolerance in the presence of different failure modes.

Given the limited research on free-swinging failures and the associated control challenges, this paper introduces a novel approach to address this issue. Specifically, it proposes the incorporation of new components, artificial tendons, to mitigate the challenges associated with free-swinging failures. Tendons, recognized for their role in transmitting force and maintaining joint stability in animals [18], serve as inspiration for the application of artificial tendons in robotics. Previous studies have demonstrated the potential of artificial tendons to facilitate joint movement and conserve energy in robot snakes and fish [19], [20]. Here, we show that the transmission of forces by artificial tendons can also be utilized to improve fault tolerance.

The structure of this paper is organized as follows: Section II introduces the design of fault-tolerant robotic arms, encompassing the design for artificial tendons, parameter settings, and the solution of the model. Section III presents results on the FTWS of planar and spatial robotic arms. Finally, Section IV concludes the paper by summarizing the key findings.

## II. MODEL AND SOLUTION

### A. Design

We introduce the incorporation of retaining rings and elastic strings on both sides of the robotic arm (see Fig. 1). The ends of the strings are fixed on the base and the last arm but are free to slide through the rings on the middle arms. These additions aim to control the movement of the failure joint through the tension and torque from the strings, which is determined by the motion of other active joints. This approach promotes the control of the passive joint, consequently enabling the end effector of the robotic arm reach its desired position. The inclusion of artificial tendons, i.e. elastic strings, enables a more versatile and stable control of the failure joint compared to gravity. Furthermore, since the joint is not actively locked, this design may provide a larger fault-tolerance workspace than the conventional method of promptly locking the joint upon detection of a fault.

Taking a planar three degree-of-freedom (DOF) robotic arm as example, we introduce a pair of supports on each arm for every joint (Fig. 1(a)). Each support is accompanied by a ring, and the elastic strings connect from the first pair of supports to the last pair, passing through rings on the middle supports, as illustrated in Fig. 1(b).

We note that the elastic strings employed here differ from the driving method used in wire-driven soft robots. In this design, the robotic arm remains joint-driven, and the elastic strings serve as auxiliary drives post-failure. Unlike wire-driven soft robots, there are no motors controlling the strings actively changing their length during the movement of the robotic arm.

For simplicity in calculations, we adopt a parameter setting with each arm being of equal length, denoted as  $l_{arm} = 1$ . The distance from the small support holding the ring to the subsequent joint is set as  $a = 0.2 \cdot l_{arm}$ . The height from the centerline of the arm to the ring is designated as  $d = 0.1 \cdot l_{arm}$ , equaling to the joint radius  $r$ . Introducing a pretension force 'tension' on the strings is necessary to prevent slackening of the elastic strings during the movement of the robotic arm. The magnitude of the pretension equal to the elastic coefficient times the stretched length of the elastic strings when all joint angles are 0.

### B. Torque on a Failed Joint

Under normal operating conditions, the servo motor on the joints can generate sufficient torque to rotate the joint to the specified angle. In the event of a free-swinging failure in a joint, where the motor's torque becomes zero, the rotation of the joint is determined by the tension acting on the ring closest to the failed joint (see Appendix A). For simplicity, the friction forces on the strings are ignored. For example, if joint 2 fails (Fig. 1(d)), the total torque  $T$  of the joint is the difference between the torques on the two strings  $T_{up}, T_{down}$ , given by the following equation:

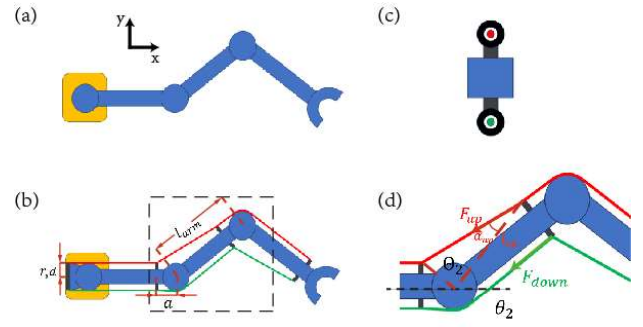


Fig. 1. (a) A regular three-link robotic arm, with arms connected and fixed to a yellow base, operates within the x-y plane. (b) Fault-tolerant robotic arm with elastic strings. The supports are shown by the thick black lines. The green and red lines represent the two elastic strings. (c) The cross-sectional view of the ring. (d) An enlarged version of the failure joint 2.

$$\begin{aligned} T &= T_{up} - T_{down} \\ &= l_{up} \cdot F_{up} \cdot \sin \alpha_{up} - l_{down} \cdot F_{down} \cdot \sin \alpha_{down} \end{aligned} \quad (1)$$

here  $l_{up}, l_{down}$  represent the distance from the rings to the center of the joint. They are constant and computed as  $l_{up} = l_{down} = \sqrt{(1-a)^2 + d^2}$ . Forces  $F_{up}, F_{down}$  are on the two elastic strings, determined by tension and angles of all the joints. Angles  $\alpha_{up}, \alpha_{down}$  are between the string and  $l_{up}, l_{down}$ , only related to the failure joint angle  $\theta_2$ . Since the angle of the failure joint is  $\theta_2 > 0$  at this time, the green string is parallel to the arm here, so we have  $l_{down} \cdot \sin \alpha_{down} = d$ , and there is a simplified equation:

$$T = T_1 - T_2 = l_{up} \cdot F_{up} \cdot \sin \alpha_{up} - d \cdot F_{down} \quad (2)$$

We take  $\alpha = \alpha_{up}$  when  $\theta_2 > 0$ . Angle  $\alpha$  can be obtained by geometric relation:

$$\begin{aligned} \sin \alpha &= \frac{a'}{\sqrt{a'^2 + b'^2 - 2a'b' \cos \Theta_2}} \sin \Theta_2 \\ \Theta_2 &= \pi - |\theta_2| - \arctan \frac{d}{a} - \arctan \frac{d}{1-a}, \\ a' &= \sqrt{a^2 + d^2}, b' = \sqrt{(1-a)^2 + d^2} \end{aligned} \quad (3)$$

In the case of  $\theta_2 < 0$ , we take  $\alpha = \alpha_{down}$  and the same equation can be obtained.

### C. Equilibrium Angles

The joint angles at which the torque  $T$  becomes zero are referred to as equilibrium angles. In the scenario where a joint experiences failure while all other joints stop moving, the failed joint will settle at one of the equilibrium angles. Our analysis of the robotic arm's behavior post-failure is predicated on the assumption that the system engages in quasi-static motion after the fault joint angle converges to the equilibrium angles.

After establishing the method to calculate the equilibrium angle ( $T = 0$ ), we proceed with a straightforward analysis of this

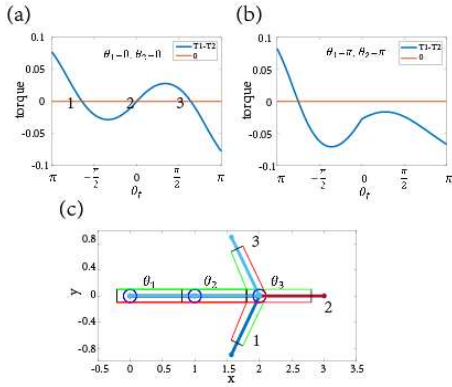


Fig. 2. (a) Net torque (blue line) on the failed joint 3 with the other two joints fixed at 0. The red line indicates  $T = 0$  and the numbers on the line indicates the equilibrium angles. (b) Net torque on the failed joint 3 with the other two joints fixed at  $\pi$ . (c) Configuration of robotic arm as joint 3 reach three equilibrium angles shown in (a).

critical parameter. When the failure joint angle  $\theta_f$  is at  $-\pi$ , both strings exert torques that simultaneously induce a counter-clockwise rotation, resulting in a positive value for  $T$ . As the angle increases, the torques from the two strings become opposite, leading to a decrease in magnitude for the torque. A similar scenario unfolds when  $\theta_f = \pi$ . Consequently, there is an overall decreasing trend in the torque as a function of the angle  $\theta_f$ , typically resulting in either one or three equilibrium angles.

For a three-joint planar robotic arm with  $a = 0.2$ , various tests with  $1.2 < tension < 2.2$  (e.g., 1.3, 1.4, 1.5, and 1.6) consistently demonstrate the aforementioned  $torque - \theta_f$  relationship. As an example, when  $tension = 1.4$  and joint 3 fails with  $\theta_f = \theta_3$ , and the other two joints are fixed at 0 (Fig. 2(a)), three equilibrium angles are evident. When the other two joints are fixed at  $\pi$ , only one equilibrium angle is observed (Fig. 2(b)). Simultaneously, these values of  $tension$  prevent the relaxation of the elastic string. We choose  $a = 0.2$ ,  $tension = 1.4$  when the robotic arm is 3-DOF.

For a 2-DOF robotic arm with  $a = 0.2$ , maintaining  $tension > 0.8$  ensures the non-relaxation of the elastic strings. In the range of  $0.8 < tension < 2$ , as the active joint angle approaches 0, the  $torque - \theta_f$  curve exhibits similarity to Fig. 2(a), while approaching  $\pi$ , the curve shape is similar to Fig. 2(b). We select  $tension = 0.9$  for 2-DOF case study.

#### D. Stability of the Equilibrium Angles

The equilibrium angles are classified into two types: stable equilibrium angles and unstable equilibrium angles. Taking the case shown in Fig. 2(a) as an example, the three equilibrium angles obtained correspond to three distinct robotic arm configurations (Fig. 2(c)). The first and third configurations can return to the original position in the case of slight perturbations, characterizing them as stable equilibrium angles. In contrast, the second configuration represents an unstable equilibrium angle. When three equilibrium angles exist, there must be two stable ones, and when there are two or one equilibrium angles, there must be one stable equilibrium angle. The reason is the following:

Since torque is continuous and must be positive when  $\theta_f = -\pi$ , and negative when  $\theta_f = \pi$ , at least one solution for the torque balance equation exists. Positive torque induces counter-clockwise rotation of the failure joint by the strings, resulting in an increase in the joint angle, while negative torque causes a decrease in the joint angle. Therefore, if the curve intersects the  $x$ -axis ( $T = 0$ ) during the decreasing phase, the torque restores the joint angle and the intersection point represents a stable equilibrium angle. Thus, all stable equilibrium points are closer to  $\pm\pi$  than unstable equilibrium points.

Hence, a relatively straightforward algorithm can be employed to identify the stable equilibrium point: when the angles of other joints are specified, for the failure joint, the torques  $T$  on both sides of the strings are calculated as the angle increases/decreases from  $\pm\pi$  to 0. The process halts when  $T$  changes its sign, and the stable equilibrium point can be pinpointed using the dichotomy method. Subsequent calculations in our work exclusively utilize the stable equilibrium angle.

### III. RESULT

#### A. Calculate the FTWS

The FTWS is determined by evaluating the workspace for each one joint after failure at any angle and subsequently establishing their intersection. For the robotic arm under study, when one joint fails, the active joints remain stationary, while the failure joint moves to a stable equilibrium angle. Consequently, the end effector successfully reaches a point within the workspace of that failure. Subsequently, the active joints undergo quasi-static motion, traversing all possible angles. The failure joint also rotates accordingly, consistently remaining at the corresponding stable equilibrium angle. We can determine the end effector position by the active and failure joints angle, representing the workspace for a specific joint failure.

We also need to consider whether all stable equilibrium angles are attainable. If a negative one is in need, we can adjust all active joints to  $\pi$  initially. Referring to Fig. 2(b), the failure joint exhibits only one stable equilibrium angle, which is negative. Subsequently, the active joints are quasi-statically adjusted back to the angles present at the time of the failure occurrence. As a result, the failure joint consistently maintains a negative stable equilibrium angle. To obtain a positive equilibrium angle, the aforementioned steps can be repeated with  $\pi$  replaced by  $-\pi$ . All stable equilibrium angles can be utilized in the calculation of FTWS.

#### B. Two-Dimensional Results

##### 1) Planer Two-Link Robotic Arm:

In the scenario where joint 1 fails, joint 2 undergoes rotation from  $-\pi$  to  $\pi$ . Each angle of joint 2 corresponds to one or two stable equilibrium angles of joint 1. By plotting the workspace corresponding to the positive and negative stable equilibrium angles of joint 1 and comparing it with the workspace corresponding to the failure of joint 2, six intersection points are identified as the FTWS of the planar two-link robotic arm with  $tension = 0.9$  and  $a = 0.2$ , as shown in Fig. 3(a). A comparison with the FTWS obtained by locking the joint upon detecting

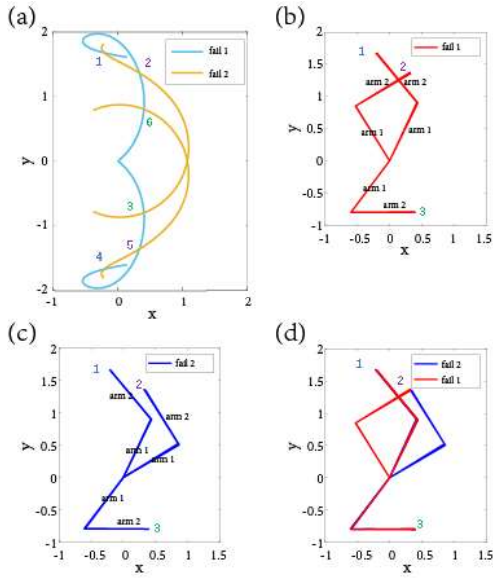


Fig. 3. (a) Workspace of the two-link robotic arm with parameters  $a = 0.20$ ,  $tension = 0.9$  when each joint fails. The light cyan line represents the workspace when the first joint fails, and the yellow line represents that of the second joint failing. Their intersection is the FTWS, the six points. (b) The robotic arm configurations when joint 1 fails, considering the end effector

free-swinging failure reveals an improvement from an empty set to six points.

Before delving into the analysis, it is essential to acknowledge a key property of the FTWS: symmetry. For a planar robotic arm with  $n$  joints,  $\vec{\theta} = (\theta_1, \theta_2, \dots, \theta_n)$ , the end points are symmetrical with respect to the  $x$ -axis when all joints assume opposite angles. When joint  $i$  fails,  $(\theta_1, \theta_2, \dots, \theta_i, \dots, \theta_n)$  and  $(-\theta_1, -\theta_2, \dots, -\theta_i, \dots, -\theta_n)$  have perfectly symmetrical positions, and the corresponding torques on the elastic strings are also perfectly symmetrical. That means when  $\theta_i$  is the equilibrium angle for  $(\theta_1, \theta_2, \dots, \theta_{i-1}, \theta_{i+1}, \dots, \theta_n)$ ,  $-\theta_i$  is also the equilibrium angle for  $(-\theta_1, -\theta_2, \dots, -\theta_{i-1}, -\theta_{i+1}, \dots, -\theta_n)$ , and the end positions of both are in the FTWS. As a result, FTWS must be symmetrical about the  $x$ -axis.

Given the symmetry, only three points 1, 2, 3 on the FTWS are analyzed. Fig. 3(b, c) illustrates the robotic arm configurations reaching points 1, 2 and 3 when the second joint and the first joint fail, respectively. These configurations are combined in Fig. 3(d). It is observed that for point 1, different joint failures yielding stable equilibrium angles result in the same robotic arm configuration. Point 3 exhibits a similar phenomenon, with the only difference being the joint angle. Point 2, however, displays different configurations for different joint failures. Further observation of the angle shows that there is  $\theta_1 = \theta_2$  when reaching point 1 and  $\theta_1 = -\theta_2$  for point 3.

Next, an analysis is conducted for situations where two failure points share the same configuration. For the case where both  $\theta_1$  and  $\theta_2$  have the same sign, let's say  $\theta_1, \theta_2 > 0$ , we have

$$l \cdot F_1^1 \cdot \sin(\alpha_1) = d \cdot F_1^2 \quad (4)$$

for joint 1 fails and

$$l \cdot F_2^1 \cdot \sin(\alpha_2) = d \cdot F_2^2 \quad (5)$$

for joint 2 fails.  $F_j^i$  represents the force on the string  $i$  when the joint  $j$  fails. Since the robotic arm shares the same configuration when either joint 1 or joint 2 fails, the stretch amount of the corresponding elastic strings is identical. Consequently, the force on the same string is equal, i.e.,  $F_1^1 = F_2^1$ ,  $i = 1, 2$ . Dividing the two equations gets:

$$\frac{\sin \alpha_1}{\sin \alpha_2} = 1 \quad (6)$$

It is obvious that  $\theta_1 = \theta_2$  satisfies (6). For a robotic arm with parameters  $tension = 0.90$ ,  $a = 0.2$ ,  $\theta_1 = \theta_2 = 1.13$  is the sole solution. However, a parameter change may introduce the additional solutions. For instance,  $tension=1.05$ ,  $a=0.2$  leads the additional solutions  $(\theta_1, \theta_2) = (1.52, 0.98)$  and  $(0.98, 1.52)$  except from the definite one,  $\theta_1 = \theta_2 = 1.29$ . The existence of this second solution is parameter-dependent, but  $\theta_1 = \theta_2 = \theta_e$  remains a constant solution. By substituting  $\theta_1 = \theta_2 = \theta_e$  into (4) and (5), the following expression is derived:

$$l \cdot F^1 \cdot \sin(\alpha_e) = d \cdot F^2 \quad (7)$$

$F^1, F^2, \alpha_e$  are only related to  $\theta_e$ . Solving this equation provides the points in the FTWS, specifically illustrated as point 1 and 4 in Fig. 3(a).

In the scenario where  $\theta_1$  and  $\theta_2$  have different signs while the two failures still share the same configuration, assuming  $\theta_1 > 0 > \theta_2$ , the following torque balance equations are formulated:

$$\begin{aligned} l \cdot F_1^1 \cdot \sin(\alpha_1) &= d \cdot F_1^2 \\ l \cdot F_2^2 \cdot \sin(\alpha_2) &= d \cdot F_2^1 \end{aligned} \quad (8)$$

When  $\theta_1 = -\theta_2$ , the stretches on both sides' strings are equal, the force on each string is equivalent, i.e.,  $F_j^i = F$ . Additionally,  $\sin \alpha_1 = \sin \alpha_2$  as  $\theta_1 = -\theta_2$ . Consequently, the two equations degenerate into one:

$$l \cdot \sin(\alpha_1) = d. \quad (9)$$

The equation implies that the two strings are parallel to the arm between the failure joint and the following pair of rings, leading to  $\theta_1 = -\theta_2 = \pi - 2 \cdot \arctan(\frac{d}{a})$ . This angle remains unaffected by the parameter  $tension$ , remarkably. Thus, two points in the FTWS must represent the end effector when  $\vec{\theta} = \pm(\pi - 2 \cdot \arctan(\frac{d}{a}), -\pi + 2 \cdot \arctan(\frac{d}{a}))$ , as illustrated by points 3 and 6 in Fig. 3(a).

When two failure conditions result in different configurations within the FTWS, as seen in point 2 of Fig. 3(d), four angles (two joint angles for each joint failure) can be obtained through four equations: two torque balance equations and two end position equations. The computed results exhibit variations dependent on the parameters  $tension$  and  $a$ . Further analysis will be conducted in future investigations to delve deeper into these findings.

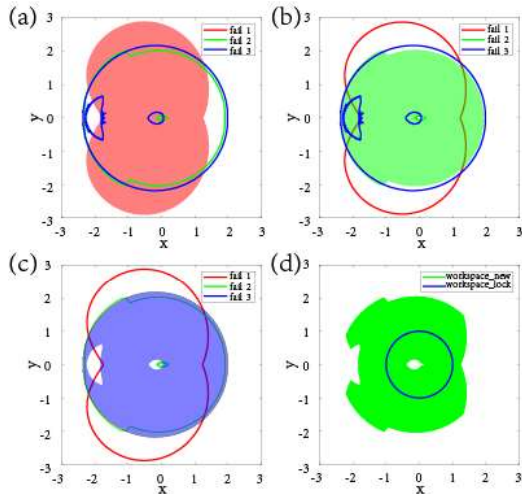


Fig. 4. (a-c) Workspace of the robotic arm when joint 1-3 fails, the red, green, blue part respectively. (d) The green part is the FTWS of the robotic arm, compared with FTWS of a traditional locked-joint fault-tolerance robotic arm, as shown in blue line.

In summary, the FTWS of a planar two-link robotic arm consists of several points on the plane. These points exhibit symmetry about the  $x$ -axis. The robotic arm reaches two of these points when the two joint angles are identical, while reaching the other two with joint angles  $\vec{\theta} = \pm(\pi - 2 \cdot \arctan(\frac{d}{a}), -\pi + 2 \cdot \arctan(\frac{d}{a}))$ . Compared to locking the free-swinging failure joint, the FTWS demonstrates expanded capabilities.

### 2) Planer Three-Link robotic arm:

Similar to the two-link robotic arm, the FTWS for a planar three-link robotic arm in the case of a single joint failure is determined by considering both positive and negative stable equilibrium angles. The FTWS is computed using the specified parameters  $tension = 1.4$  and  $a = 0.2$ . Fig. 4(a) illustrates the workspace in the event of joint 1 failure. By adjusting the angles of joints 2 and 3, the robotic arm's end effector can reach all points within this workspace. Fig. 4(b) displays the workspace when joint 2 fails, with a small section removed in the middle. The workspace of joint 3 failure is depicted in Fig. 4(c), where, in addition to the region near the origin, there is a crescent-shaped area in the negative direction of the  $x$ -axis that remains unreachable. The intersection of these workspaces forms the FTWS shown in Fig. 4(d). In contrast to the FTWS of a locked-joint robotic arm, which consists of points on a circle with a radius of 1, the FTWS expands from a curve to an annular region, transitioning from one-dimensional to two-dimensional.

### C. Three-Dimensional Result

#### 1) Design for the Three-Dimensional Robotic Arm:

In addition to the design considerations for planar robotic arms, we also explored the configuration of a spatial robotic arm. For a spatial robotic arm with Denavit-Hartenberg (D-H) parameters as shown in Table I, the incorporation of artificial tendons involves adding cross structures to the positions originally occupied by the supports, as illustrated in Fig. 5(b). The tops of these structures function as rings, maintaining a distance  $d$  from the center of the arm. The elastic strings traverse

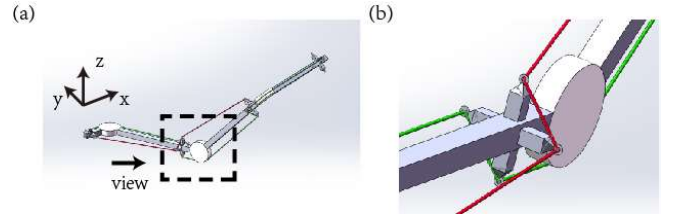


Fig. 5. (a) Configuration of a spatial robotic arm with elastic strings. The discs represent joints, with the first joint on the left. The gray part denotes the arms, while the red and green lines on both sides of the robotic arm represent elastic strings. (b) Crossed structures hold the rings where the elastic strings pass through.

TABLE I. D-H PARAMETER FOR THE ROBOTIC ARM

$a_i$	$\alpha_i$	$d_i$	$\theta_i$
1	$\frac{\pi}{2}$	0	$\theta_1$
1	$\frac{\pi}{2}$	0	$\theta_2$
1	0	0	$\theta_3$

from one ring to another on the cross structure and then connect to the subsequent joint. The segment of elastic strings situated between two cross structures lies in the motion plane of the joint, and the two-dimensional equation can be extrapolated to the three-dimensional space. Fig. 5(a) provides a schematic representation of the spatial robotic arm.

#### 2) Calculation for FTWS of 3D Three-Link Robotic Arm:

When a single joint fails in the three-dimensional three-link robotic arm, the resulting workspace consists of surfaces. The intersection of failures in three different joints forms a set of points, representing the FTWS of three-dimensional robotic arm. In order to accurately calculate the position of each point and the corresponding joint angles, the following algorithm is devised:

- I. Calculate the equilibrium angle when joint 1 fails, with joints 2 and 3 varying in the range from  $-\pi$  to  $\pi$  with an interval of  $\Delta\theta$ . A similar process is employed when joint 2 or 3 fails.
- II. Determine the end effector position using the angles obtained in step I, denoted as points set 1, 2, and 3 for each joint failure.
- III. Identify points from points set 1 that are close to both points in sets 2 and 3, where the distance between points is less than a precision parameter  $\epsilon$ . The obtained points constitute the approximate FTWS. simultaneously, the approximate joint angles  $\vec{\theta}^1 = (\theta_1, \theta_2, \theta_3)$  for joint 1 failure is gotten.
- IV. Find the points in points set 2 and 3 that are closest to those in the approximate FTWS. Obtain approximate joint angles  $\vec{\theta}^2 = (\theta_1, \theta_2, \theta_3)$  for joint 2 failure and  $\vec{\theta}^3 = (\theta_1, \theta_2, \theta_3)$  for joint 3 failure.
- V. Use the Newton method to derive the real solution from each approximate solution  $\vec{\theta}^1, \vec{\theta}^2, \vec{\theta}^3$ .

- VI. Verify the physical feasibility of the real solution. Ensure that every joint angle in  $\bar{\theta}^1, \bar{\theta}^2, \bar{\theta}^3$  lies in the range  $[-\pi, \pi]$ .

Steps I-IV are intended for calculating the approximate solution. When  $n = \frac{2\pi}{\Delta\theta} = 600$ , we take  $\epsilon = 0.10 > \sqrt{59}\Delta\theta$  to find the approximate solution. This choice of  $\epsilon$  ensures that the approximate solution remains close to the real solution, with the distance between the end effector of the two solutions being less than  $\epsilon/\sqrt{2}$  (see Appendix B for details).

### 3) Results and Analysis for FTWS of 3D Three-Link Robotic Arm:

The resulted FTWS includes all points on the circle of radius 1 and additional points outside the circle (Fig. 6(a)). Such FTWS is also greater than the FTWS with a locked-joint strategy, which is only a circle. Like the planar two-link robotic arm, symmetry of the robotic arm results in a symmetrical FTWS about the  $x$ -axis. We will analyze the points on the circle first and discuss how the robotic arm reaches these points. Both locked-joint and free-swinging failure will be discussed and compared to each other.

For a locked-joint robotic arm, in the extreme case where the second joint fails at  $\pm\pi$ , the end effector is confined to the circle. Therefore, points outside the circle cannot be part of the FTWS of the locked-joint robotic arm. Next, we discuss how the robotic arm reaches these points when failures occur at individual joints. If the 1st or 3rd joint fails and locks at any angle, the 2nd joint can be controlled to stay at an angle of  $\pi$ . The end effector rotates along the circle as the other active joint moves from  $-\pi$  to  $\pi$ , eventually returning to the initial point. Similarly, when joint 2 fails and locks at any angle, setting joint 3 to  $\pi$  allows the end effector to traverse all points on the circle as the 1st joint moves from  $-\pi$  to  $\pi$ .

In the case of a free-swinging joint failure, the angle of the failure joint changes as the other joint moves. Fortunately, when the first or third joint fails, the same process can be applied as in the locked-joint failure. The failure joint always has a negative stable equilibrium angle, gradually decreasing as the unfixed active joint becomes larger. This overall effect promotes the rotation of the end effector, causing it to rotate slightly more than the entire circle. When the second joint fails, with the third joint stopped at  $\pi$ , the end effector coincides with the second joint. As the first joint moves from  $-\pi$  to  $\pi$ , the end rotates once along the circle. Consequently, the circle also constitutes part of the FTWS of a free-swinging fault-tolerant robotic arm.

The FTWS for a free-swinging failure also includes points outside the circle, which are inaccessible for locked-joint failures. For these points, the robotic arm's configuration can be expressed in terms of joint angles, denoted as  $\bar{\theta} = (\theta_1, \theta_2, \theta_3)$ . Each point can be achieved by at most two sets of angles:  $(\theta_1, \theta_2, \theta_3)$  and  $(\theta_1', \theta_2, \theta_3)$  (see Appendix C). Similar to the analysis conducted on the planar two-link robotic arm, we examine the robotic arm experiencing three different joint faults reaching a specific point on the FTWS in both the same and different configurations.

By symmetry, we only need to discuss the case  $\theta_1 > 0$ . When the same configuration is used and all the joints are in the same

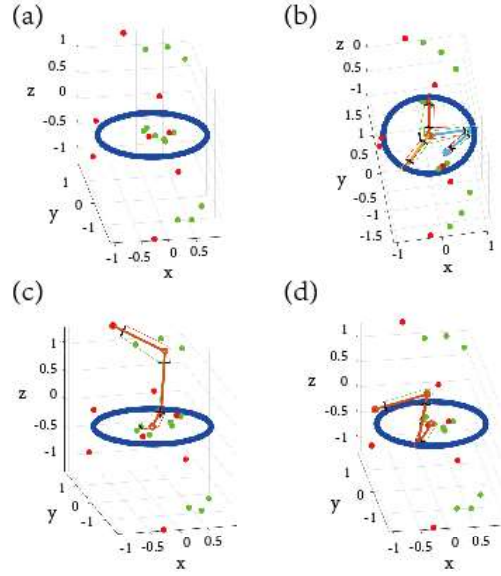


Fig. 6. (a) FTWS of the spatial robotic arm, including a circle of radius 1 (blue) and scattered points (red and green). Red points refer to those reached by the same configuration when different joints fail. Green points refer to those reached by different configurations when different joints fail. (b) Configurations of the robotic arm for reaching the point (1,0,0) on the circle when each joint fails. The orange robotic arm fails at the first joint, the blue one fails at the second joint and the red one fails at the third joint. The third arm of the yellow and orange robotic arms is obscured by the blue robotic arm. (c-d) The robotic arm reaches points with same configuration when different joints fail. (c) shows the configuration when all the joint angles are equal. (d) shows one configuration when all the joint angles are not equal.

sign  $\theta_2, \theta_3 > 0$ . Similar to the explanation provided for the planar two-link robotic arm, the force on the same string is equal when any joint fails. The equations for the three different failure cases are:

$$\begin{aligned} l \cdot F_1^1 \cdot \sin(\alpha_1) &= d \cdot F_1^2 \\ l \cdot F_2^1 \cdot \sin(\alpha_2) &= d \cdot F_2^2 \\ l \cdot F_3^1 \cdot \sin(\alpha_3) &= d \cdot F_3^2 \\ F_1^i &= F_2^i = F_3^i, i = 1, 2, 3 \end{aligned} \quad (10)$$

Consequently,  $\sin\alpha_1 = \sin\alpha_2 = \sin\alpha_3$ . Obviously  $\theta_1 = \theta_2 = \theta_3$  is a solution (see Fig. 6(c)). As we have explained in planer two-link robotic arm, there can be other solutions for the equation for some system parameters.

When the three failed joints exhibit different signs, but the robotic arms remain in the same configuration, the case of  $\theta_1 > 0, \theta_2, \theta_3 < 0$  leads to the following equations:

$$\begin{aligned} l \cdot F_1^1 \cdot \sin(\alpha_1) &= d \cdot F_1^2 \\ l \cdot F_2^2 \cdot \sin(\alpha_2) &= d \cdot F_2^1 \\ l \cdot F_3^2 \cdot \sin(\alpha_3) &= d \cdot F_3^1 \\ F_1^i &= F_2^i = F_3^i, i = 1, 2, 3 \end{aligned} \quad (11)$$

Subsequently, we derive the following relations:

$$\begin{aligned}\sin \alpha_2 &= \sin \alpha_3 \\ \sin \alpha_1 \cdot \sin \alpha_2 &= \frac{d^2}{l^2}\end{aligned}\quad (12)$$

$\theta_2 = \theta_3$  obviously satisfies the equation. Therefore, for the scenario where two joints have the same sign and the other joint has a different sign, two joint angles are equal is a solution. This corresponds to the six red dots in Fig. 6(d). The other two red dots are the cases where all joint angles are identical.

In the situation where the three faults converge at a point on the FTWS in two configurations (green points), we have not found analytical relations between the joints. They might just occur by coincidence.

#### IV. CONCLUSION

This paper investigates the fault-tolerance of robotic arms under free-swinging failure, employing elastic strings to control the failed joints. The manipulation is achieved by regulating the force and torque exerted by the elastic strings on the arms through other functioning joints.

The FTWS for both planar and spatial robotic arms is computed and compared with the FTWS obtained by directly locking the failure joint. It is noted that robotic arms equipped with elastic strings demonstrate an increased FTWS. In the context of the planar two-link robotic arm, the FTWS undergoes a transition from an empty set to multiple points in the plane. Similarly, for the planar three-link robotic arm, the FTWS expands from points on a circle with a radius of 1 to an annular region. In the case of the spatial three-link robotic arm, the FTWS encompasses additional scattered points in space, expanding upon the foundation of a circle with a radius of 1.

A detailed analysis of how the robotic arm attains FTWS during a failure event has been conducted. Examination of points within the FTWS, including configurations and joint angles, reveals that in both the planar two-link and spatial three-link robotic arms, certain points are reached by the robotic arm in identical configurations when different joints fail. Remarkably, there are many instances where all joint angles are equal.

The fault-tolerant robotic arm proposed in this paper presents a novel approach to address free-swinging failure and has the potential for extension to other fault-tolerant machines. By incorporating a simple device without increasing degrees of freedom, the machine's fault-tolerance can be significantly improved.

#### APPENDIX A

##### CALCULATION OF THE TORQUE

In the event of a free-swinging failure in a joint, the failure joint divides the robotic arm into two parts. We need to compute the torque applied on the joint from the strings on the end-effector side. When the string contacts the robotic arm on a ring, the net force is the sum of the tensions from two sides of the ring (Fig. 7(a)). When the string contacts the robotic arm on a joint (Fig. 7(b)), the force exerted by the string on the joint can be considered as multiple pressures  $N_i$ . Each  $N_i$  is the resultant

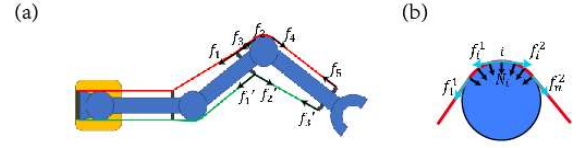


Fig. 7. (a) The forces exerted by the strings on the part of robotic arm containing the end effector when the second joint fails. (b) When one string contacts with one joint, the forces exerted by the string are represented by the black lines. The tensions in the string are indicated by the blue lines.

force of the two tensions,  $f_i^1$  and  $f_i^2$ . Observing that the resultant torque generated by  $f_i^1$  and  $f_i^2$  is zero, the total torque exerted by the string on the joint can be all attributed to  $f_1^1$  and  $f_n^2$ .

If the second joint fails (Fig. 7(a)), the part of robotic arm containing the end effector includes the second arm, the third joint, the third arm, and the end effector. The green string connects this part through two rings, generating three forces:  $f_1^1$ ,  $f_2^1$ , and  $f_3^1$ . Forces  $f_2^1$  and  $f_3^1$  are on the same segment of string, and their resultant torque on the failure joint is zero. So that the total torque of this string on the failure joint is determined by  $f_1^1$ . The red string generates  $f_1, f_2, f_5$  at the rings and  $f_3, f_4$  at the joint. The torques generated by forces  $f_2, f_3$  cancel each other out, so as to forces  $f_4, f_5$ . The total torque of the red string on the failure joint is determined by  $f_1$ . The force applied by the string on the failure joint does not have any effect on its rotation, since the forces are pointing to the rotational axis of the joint.

#### APPENDIX B

##### CHOICE OF $\epsilon$

In the initial two steps of the algorithm, the workspace for joints 1, 2, and 3 failure is determined individually. Given that we take an interval of  $\Delta\theta$  for the functioning joints, the obtained workspace is a non-Cartesian mesh within the actual 3D space. The actual intersection of the workspaces might be between two vertices of the mesh (Fig. 8). Here we show that the distance  $\Delta l$  from this point to the nearest mesh vortex follows the relationship:  $\Delta l < \sqrt{59/2}\Delta\theta$ .

By utilizing the Denavit-Hartenberg (DH) parameters, the transformation matrices (A matrices) are expressed as following:

$$\begin{aligned}A_1 &= \begin{bmatrix} \cos \theta_1 & 0 & \sin \theta_1 & \cos \theta_1 \\ \sin \theta_1 & 0 & -\cos \theta_1 & \sin \theta_1 \\ 0 & 1 & 0 & 0 \\ 0 & 0 & 0 & 1 \end{bmatrix}, \\ A_2 &= \begin{bmatrix} \cos \theta_2 & 0 & -\sin \theta_2 & \cos \theta_2 \\ \sin \theta_2 & 0 & \cos \theta_2 & \sin \theta_2 \\ 0 & -1 & 0 & 0 \\ 0 & 0 & 0 & 1 \end{bmatrix}, \\ A_3 &= \begin{bmatrix} \cos \theta_3 & -\sin \theta_3 & 0 & \cos \theta_3 \\ \sin \theta_3 & \cos \theta_3 & 0 & \sin \theta_3 \\ 0 & 0 & 1 & 0 \\ 0 & 0 & 0 & 1 \end{bmatrix},\end{aligned}\quad (13)$$

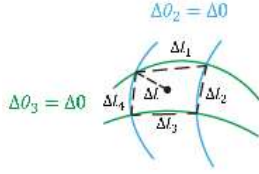


Fig. 8. Schematics of the workspace when joint 1 fails. The point in the middle is one point of FTWS. Green (blue) lines represent the route of the end effector when the third (second) joint is fixed and the other joint can rotate freely. The four intersection points are obtained in step II in the algorithm. The distance of each other is  $\Delta l_i$ , and the distance from the point in FTWS to the nearest vertex in the mesh is  $\Delta l$ .

So we get the T matrix

$$T = A_1 \cdot A_2 \cdot A_3 \quad (14)$$

and kinematic formula

$$\begin{pmatrix} \dot{x} \\ \dot{y} \\ \dot{z} \end{pmatrix} = J_v \begin{pmatrix} \dot{\theta}_1 \\ \dot{\theta}_2 \\ \dot{\theta}_3 \end{pmatrix} \quad (15)$$

Here  $J_v$  is the first three rows of the Jacobian matrix, calculated from T matrix,

$$J_v = \begin{bmatrix} \frac{\partial x}{\partial \theta_1} & \frac{\partial x}{\partial \theta_2} & \frac{\partial x}{\partial \theta_3} \\ \frac{\partial y}{\partial \theta_1} & \frac{\partial y}{\partial \theta_2} & \frac{\partial y}{\partial \theta_3} \\ \frac{\partial z}{\partial \theta_1} & \frac{\partial z}{\partial \theta_2} & \frac{\partial z}{\partial \theta_3} \end{bmatrix}, \quad (16)$$

$$\begin{aligned} \frac{\partial x}{\partial \theta_1} &= -\sin \theta_1 - \sin \theta_1 \cos \theta_2 - \sin \theta_3 \cos \theta_1 \\ &\quad - \sin \theta_1 \cos \theta_2 \cos \theta_3 \\ \frac{\partial x}{\partial \theta_2} &= -\sin \theta_2 \cos \theta_1 - \cos \theta_1 \sin \theta_2 \cos \theta_3 \\ \frac{\partial x}{\partial \theta_3} &= -\cos \theta_3 \sin \theta_1 - \cos \theta_1 \cos \theta_2 \sin \theta_3 \\ \frac{\partial y}{\partial \theta_1} &= \cos \theta_1 - \sin \theta_1 \sin \theta_1 + \cos \theta_1 \cos \theta_2 \\ &\quad + \cos \theta_1 \cos \theta_2 \cos \theta_3 \\ \frac{\partial y}{\partial \theta_2} &= -\sin \theta_1 \sin \theta_2 - \sin \theta_1 \sin \theta_2 \cos \theta_3 \\ \frac{\partial y}{\partial \theta_3} &= \cos \theta_1 \cos \theta_3 - \sin \theta_1 \cos \theta_2 \sin \theta_3 \\ \frac{\partial z}{\partial \theta_1} &= 0 \\ \frac{\partial z}{\partial \theta_2} &= \cos \theta_2 + \cos \theta_2 \cos \theta_3 \\ \frac{\partial z}{\partial \theta_3} &= -\sin \theta_2 \sin \theta_3 \end{aligned}$$

When  $\theta_2$  is controlled to fix at different values, varying  $\theta_3$ , the robotic arm's end effector traces out a set of blue lines, as illustrated in Fig. 8.  $\Delta\theta_2$  represents the interval between these values. The green lines correspond to controlling  $\theta_3$  at certain fixed values. The intersections of the blue lines and green lines

form the mesh. The vertices on the mesh are the discrete points we compute in the algorithm. In one blue line or one green line, there is  $\Delta\theta_2 = 0$  or  $\Delta\theta_3 = 0$ . From Fig. 8 we get:

$$\Delta l_i^2 = \Delta x_i^2 + |\Delta y_i^2 + \Delta z_i^2, i = 1, 2, 3, 4 \quad (17)$$

For  $\Delta l_1$  or  $\Delta l_3$ , we have  $\Delta\theta_2 = \Delta\theta$ ,  $\Delta\theta_3 = 0$ . For  $\Delta l_2$  or  $\Delta l_4$ , we have  $\Delta\theta_3 = \Delta\theta$  and  $\Delta\theta_2 = 0$ .

$$\begin{aligned} |\Delta x_i| &= \left| \frac{\partial x}{\partial \theta_1} \Delta\theta_1 + \frac{\partial x}{\partial \theta_2} \Delta\theta_2 + \frac{\partial x}{\partial \theta_3} \Delta\theta_3 \right| \\ &\leq \left| \frac{\partial x}{\partial \theta_1} \right| \Delta\theta_1 + \left| \frac{\partial x}{\partial \theta_2} \right| \Delta\theta_2 + \left| \frac{\partial x}{\partial \theta_3} \right| \Delta\theta_3 \\ |\Delta y_i| &\leq \left| \frac{\partial y}{\partial \theta_1} \right| \Delta\theta_1 + \left| \frac{\partial y}{\partial \theta_2} \right| \Delta\theta_2 + \left| \frac{\partial y}{\partial \theta_3} \right| \Delta\theta_3 \\ |\Delta z_i| &\leq \left| \frac{\partial z}{\partial \theta_1} \right| \Delta\theta_1 + \left| \frac{\partial z}{\partial \theta_2} \right| \Delta\theta_2 + \left| \frac{\partial z}{\partial \theta_3} \right| \Delta\theta_3 \end{aligned} \quad (18)$$

When one of joint 2 and joint 3 is controlled to stop at one angle while the other change  $\Delta\theta$ , it is observed that the change of the failure joint  $\Delta\theta_1$  is consistently smaller than  $\Delta\theta$ . Consequently, when joint 1 fails, we find:

$$\begin{aligned} |\Delta x_i| &\leq \left| \frac{\partial x}{\partial \theta_1} \right| \Delta\theta_1 + \left| \frac{\partial x}{\partial \theta_2} \right| \Delta\theta_2 + \left| \frac{\partial x}{\partial \theta_3} \right| \Delta\theta_3 \\ &\leq 3\Delta\theta_1 + 2\Delta\theta_2 + 2\Delta\theta_3 \\ &< 5\Delta\theta \\ |\Delta y_i| &\leq 3\Delta\theta_1 + 2\Delta\theta_2 + 2\Delta\theta_3 \\ &< 5\Delta\theta \\ |\Delta z_i| &\leq 0\Delta\theta_1 + 2\Delta\theta_2 + \Delta\theta_3 \\ &< 2\Delta\theta \end{aligned} \quad (19)$$

If any one joint fails, one of  $\Delta\theta_1$ ,  $\Delta\theta_2$ ,  $\Delta\theta_3$  is set to 0, another is assigned the value of  $\Delta\theta$ , and the remaining one is constrained to be smaller than  $\Delta\theta$ . Under these conditions, the result is obtained as follows:  $|\Delta x_i| < 5\Delta\theta$ ,  $|\Delta y_i| < 5\Delta\theta$ ,  $|\Delta z_i| < 3\Delta\theta$ ,  $|\Delta l_i| < \sqrt{59}\Delta\theta$ . The small region surrounding the point within the FTWS can be approximated as a plane when  $\Delta\theta$  is sufficiently small. In this scenario, the geometric relationship assures us that  $\Delta l < \sqrt{59/2}\Delta\theta$ .

Here,  $\Delta l$  represents the distance from the point in FTWS to the nearest vortex in the mesh. Additionally, the distance between two closest vertices from different meshes, such as the mesh associated with joint 1 failure and joint 2 failure, should be smaller than  $\sqrt{2}\Delta l$ .

## APPENDIX C

### AT MOST TWO SETS OF SOLUTIONS REACHING POINTS OUTSIDE THE CIRCLE

Utilizing the T-matrix from (14), we obtain the equation for the end effector position of the robotic arm:

$$\begin{aligned}
x &= \cos \theta_1 + \cos \theta_1 \cos \theta_2 \\
&\quad - \sin \theta_1 \sin \theta_3 + \cos \theta_1 \cos \theta_2 \cos \theta_3 \\
y &= \sin \theta_1 + \cos \theta_1 \sin \theta_3 \\
&\quad + \sin \theta_1 \cos \theta_2 + \sin \theta_1 \cos \theta_2 \cos \theta_3 \\
z &= \sin \theta_2 + \sin \theta_2 \cos \theta_3
\end{aligned} \tag{20}$$

Using  $r^2 = x^2 + y^2$ , we obtain:

$$r^2 = 1 + 2 \cos \theta_2 (1 + \cos \theta_3) + \sin^2 \theta_3 + \cos^2 \theta_2 (1 + \cos \theta_3)^2 \tag{21}$$

$$z = \sin \theta_2 + \sin \theta_2 \cos \theta_3 \tag{22}$$

We observe that when  $\cos \theta_3 = -1$ , i.e.,  $\theta_3 = \pm\pi$ ,  $(r^2, z) = (1, 0)$ . The end effector of the robotic arm is located on the circle, consistent with our previous analysis of points on the circle.

When  $\cos \theta_3 \neq -1$ , (22) can be rewritten as follows:

$$\sin \theta_2 = \frac{z}{1 + \cos \theta_3} \tag{23}$$

Substituting back into (21), we have:

$$r^2 = 3 + 2\sqrt{(1 + \cos \theta_3)^2 - z^2} + 2 \cos \theta_3 - z \tag{24}$$

for  $\theta_2 \in [-\frac{\pi}{2}, \frac{\pi}{2}]$  and

$$r^2 = 3 - 2\sqrt{(1 + \cos \theta_3)^2 - z^2} + 2 \cos \theta_3 - z \tag{25}$$

for  $\theta_2 \in [-\pi, -\frac{\pi}{2}], [\frac{\pi}{2}, \pi]$ .

Let  $t = \cos \theta_3 + 1$ , then  $t \in (0, 2)$  as  $\theta_3 \in (-\pi, \pi)$ . Equation (24) and (25) become

$$r^2 = 1 \pm 2\sqrt{t^2 - z^2} + 2t - z^2 \tag{26}$$

Eliminate the square root and rewrite the above expression:

$$t = \frac{4z^2 + (z^2 - 1 + r^2)^2}{4(z^2 - 1 + r^2)} \tag{27}$$

For one end effector position,  $r^2$  and  $z$  are unique, and we get only one  $t$  from (27). Correspondingly, there are at most two  $\theta_3$  satisfying (24) and (25). For one  $t = \cos \theta_3 + 1$ , we can find only one  $\theta_2 \in [-\pi, \pi]$  that satisfying (23). When both  $\theta_2$  and  $\theta_3$  are determined, rewriting the  $x$  and  $y$  terms in (20) yields:

$$\begin{aligned}
\begin{bmatrix} -p & q \\ q & p \end{bmatrix} \begin{bmatrix} \sin \theta_1 \\ \cos \theta_1 \end{bmatrix} &= \begin{bmatrix} x \\ y \end{bmatrix} \\
p &= \sin \theta_3 \\
q &= 1 + \cos \theta_2 + \cos \theta_2 \cos \theta_3
\end{aligned} \tag{28}$$

The determinant of the coefficient matrix is:

$$\begin{vmatrix} -p & q \\ q & p \end{vmatrix} = -p^2 - q^2 < 0 \tag{29}$$

This implies that (28) has a unique solution, i.e., for each set of  $(x, y, z)$ , when  $\theta_2$  and  $\theta_3$  are determined, there exists only one  $\theta_1$ .

In summary, we first determine that at most two  $\theta_3$  values to reach a point outside the circle. Then we established that only one  $\theta_2$  for the two  $\theta_3$ . For each set of  $(\theta_2, \theta_3)$ , there is a unique  $\theta_1$ . Therefore, the joint angles have at most two sets of solutions:  $(\theta_1, \theta_2, \theta_3)$  and  $(\theta_1', \theta_2, \theta_3)$ .

## REFERENCES

- [1] F. Pierrot, E. Dombre, E. Dégoulange, L. Urbain, P. Caron, S. Boudet, J. Garipety, and J.-L. M'egnien, "Hippocrate: A safe robot arm for medical applications with force feedback," *Medical Image Analysis*, vol. 3, no. 3, pp. 285–300, 1999.
- [2] T. Rybus, "Obstacle avoidance in space robotics: Review of major challenges and proposed solutions," *Progress in Aerospace Sciences*, vol. 101, pp. 31–48, 2018.
- [3] O. Khatib, X. Yeh, G. Brantner, B. Soe, B. Kim, S. Ganguly, H. Stuart, S. Wang, M. Cutkosky, A. Edsinger et al., "Ocean one: A robotic avatar for oceanic discovery," *IEEE Robotics & Automation Magazine*, vol. 23, no. 4, pp. 20–29, 2016.
- [4] R. Bogue, "Robots in the nuclear industry: a review of technologies and applications," *Industrial Robot: An International Journal*, vol. 38, no. 2, pp. 113–118, 2011.
- [5] S. Cheng and B. Dhillon, "Reliability and availability analysis of a robot-safety system," *Journal of Quality in Maintenance Engineering*, vol. 17, no. 2, pp. 203–232, 2011.
- [6] J. Carlson and R. R. Murphy, "How ugv's physically fail in the field," *IEEE Transactions on robotics*, vol. 21, no. 3, pp. 423–437, 2005.
- [7] A. A. Almarkhi, A. A. Maciejewski, and E. K. Chong, "An algorithm to design redundant manipulators of optimally fault-tolerant kinematic structure," *IEEE Robotics and Automation Letters*, vol. 5, no. 3, pp. 4727–4734, 2020.
- [8] M. Plooij, G. Mathijssen, P. Cherelle, D. Lefeber, and B. Vanderborght, "Lock your robot: A review of locking devices in robotics," *IEEE Robotics & Automation Magazine*, vol. 22, no. 1, pp. 106–117, 2015.
- [9] K. M. Ben-Gharbia, A. A. Maciejewski, and R. G. Roberts, "Modifying the kinematic structure of an anthropomorphic arm to improve fault tolerance," in *2015 IEEE International Conference on Robotics and Automation (ICRA)*. IEEE, 2015, pp. 1455–1460.
- [10] B. Xie and A. A. Maciejewski, "Structure and performance analysis of the 7! robots generated from an optimally fault tolerant jacobian," *IEEE Robotics and Automation Letters*, vol. 2, no. 4, pp. 1956–1963, 2017.
- [11] R. S. Jamisola, A. A. Maciejewski, and R. G. Roberts, "Failure-tolerant path planning for kinematically redundant manipulators anticipating locked-joint failures," *IEEE Transactions on Robotics*, vol. 22, no. 4, pp. 603–612, 2006.
- [12] M. Hattori and H. Yabuno, "Reachable area of an underactuated space manipulator subjected to simple spinning: Application of bifurcation control under high-frequency excitation," *Nonlinear Dynamics*, vol. 51, pp. 345–353, 2008.
- [13] M. Isaksson, K. Marlow, A. Maciejewski, and A. Eriksson, "Novel fault-tolerance indices for redundantly actuated parallel robots," *Journal of Mechanical Design*, vol. 139, no. 4, p. 042301, 2017.
- [14] J. D. English and A. A. Maciejewski, "Failure tolerance through active braking: A kinematic approach," *The International Journal of Robotics Research*, vol. 20, no. 4, pp. 287–299, 2001.
- [15] J. D. English and A. A. Maciejewski, "Fault tolerance for kinematically redundant manipulators: Anticipating free-swinging joint failures," *IEEE Transactions on Robotics and Automation*, vol. 14, no. 4, pp. 566–575, 1998.
- [16] C. J. Paredis and P. K. Khosla, "Designing fault-tolerant manipulators: How many degrees of freedom?" *The international journal of robotics research*, vol. 15, no. 6, pp. 611–628, 1996.

- [17] J. D. English and A. A. Maciejewski, "Robotic workspaces after a free-swinging failure," *Journal of Intelligent and Robotic Systems*, vol. 19, pp. 55–72, 1997.
- [18] J. H.-C. Wang, "Mechanobiology of tendon," *Journal of biomechanics*, vol. 39, no. 9, pp. 1563–1582, 2006.
- [19] D. Xia, W. Chen, and J. Liu, "Using biological spring to improve propulsive efficiency for fishlike robot," in *2008 IEEE International Conference on Mechatronics and Automation*. IEEE, 2008, pp. 137–142.
- [20] A. Kakogawa, S. Jeon, and S. Ma, "Stiffness design of a resonance-based planar snake robot with parallel elastic actuators," *IEEE Robotics and Automation Letters*, vol. 3, no. 2, pp. 1284–1291, 2018.